Applied Catalysis B: Environmental 308 (2022) 121227

Contents lists available at ScienceDirect

Applied Catalysis B: Environmental

journal homepage: www.elsevier.com/locate/apcatb

CdS/ethylenediamine nanowires 3D photocatalyst with rich sulfur vacancies for efficient syngas production from CO_2 photoreduction

Tong Tian [a,1], Xiaoyan Jin [a,1], Neng Guo [a], Huiquan Li [a,*], Yan Han [a], Yupeng Yuan [b,*]

[a] Anhui Provincial Key Laboratory for Degradation and Monitoring of Pollution of the Environment, School of Chemistry and Materials Engineering, Fuyang Normal University, Fuyang 236037, PR China

[b] School of Materials Science and Engineering, Anhui University, Hefei 230601, PR China

ARTICLE INFO

Keywords:
CdS/EDA nanowires
Three-dimensional
Sulfur vacancies
Syngas production
CO_2 photoreduction

ABSTRACT

Herein, CdS/ethanediamine (protonated) hybrid nanowires (CdS/EDA NW) three-dimensional (3D) network structure photocatalysts with tunable sulfur vacancy concentrations were fabricated. The protonated EDA molecules modified on the surafce of CdS to assemble into 3D structure with large specific surface area can not only effectively capture visible light, but also significantly enhance the separation and transportation of charge carriers. And EDA is also conducive to CO_2 adsorption. Meanwhile, the rich sulfur vacancies (V_S-R) on the surface of CdS/EDA NW can trap more photogenerated electrons to further prolong carries lifetime as well as effectively promote the hydrogen adsorption and CO_2 activation. Hence, the V_S-R mediated 3D CdS/EDA NW exhibits the high visible light photocatalytic syngas CO and H_2 formation rate of 115.6 and 959.4 μmol g^{-1} h^{-1} (CO: H_2 = 1: 8.3) respectively. This work provides a promising idea to design efficient catalysts through multiple collaborative strategies for syngas production via CO_2 photoreduction.

1. Introduction

The consumption of fossil fuels has generated the massive CO_2 emission, which causes the severe greenhouse effect during the past decades [1–3]. To reduce CO_2 concentration, photocatalytic CO_2 reduction reactions can store and convert intermittent solar energy in the form of syngas (CO + H_2), which are the subsequent critical feedstocks to produce high value-added chemicals by Fischer-Tropsch processes, and thus has garnered intensive attentions in the past years [4,5]. Among the semiconductor materials reported for CO_2 photoreduction, CdS has been a focus of research due to its wide visible light absorption as well as suitable energy position [6,7]. However, the photocatalytic efficiency of CdS is still low due to severe photocorrosion in the process of photocatalytic reaction and the weak CO_2 activation as CO_2 molecules are chemically inert, as well as the high recombination rate of photogenerated charge carriers [8–10]. Especially, it is difficult to control the yield ratio of CO/H_2 in the process of CO_2 photoreduction. The higher the ratio of CO/H_2 generated during the reaction, the more conducive to the subsequent thermochemical conversion [4]. Therefore, exploring a strategy for the effective CO_2 adsorption and activation as well as depressed charge recombination is highly favorable yet challenging to realize the increased and tunable syngas production from CO_2 photoreduction over CdS.

It is well known that the defect state, microstructures, exposed facets, specific surface area, hybrid structures of semiconductor materials play a vital role in the photocatalytic activity, which control the electronic structure, photoinduced charge separation and charge-transfer kinetics [11–14]. The hybrid inorganic/organic materials have great potential to break through the bottlenecks of photocatalytic efficiency due to the unique structures and excellent physicochemical performance [14]. In particular, the functional organic small molecules with amino groups modified on the surface of photocatalysts can also significantly promote the charges transfer and enhance the adsorption of CO_2, and finally boost the conversion efficiency [15,16]. Notably, vacancy engineering has stood out as the effective strategy to increase the efficiency of photocatalytic CO_2 reduction in recent years [17]. The present results suggest that the surface vacancies of photocatalysts can capture the photo-excited electrons to effectively prevent the recombination of photogenerated carriers, and thus strengthening the photocatalytic performance [18,19]. Meanwhile, the surface vacancies also can serve as catalytic active sites for hydrogen adsorption, as well as CO_2 adsorption and activation which lower the activation energy of CO_2 to form

* Corresponding authors.
E-mail addresses: huiquanli0908@163.com (H. Li), yupengyuan@ahu.edu.cn (Y. Yuan).

[1] These authors contributed equally to this work.

https://doi.org/10.1016/j.apcatb.2022.121227
Received 16 December 2021; Received in revised form 19 January 2022; Accepted 16 February 2022
Available online 18 February 2022
0926-3373/© 2022 Elsevier B.V. All rights reserved.

important intermediates [20,21]. And the introduction of vacancy engineering is also capable of regulating the electronic structure of photocatalysts to improve the reduction ability of photogenerated electrons [22,23]. Moreover, 3D network structure has the large specific surface area and maximizes the utilization of incident photons through the multiple reflections within the interconnected framework [24]. Hence, it is necessary to design 3D CdS-based inorganic/organic hybrid materials with controllable surface vacancy concentrations to achieve efficient photocatalytic syngas production from CO_2 and H_2O, to clarify the relationship between structure and photocatalytic performance, and to further explore its photocatalytic mechanism.

Herein, we firstly synthesized 3D network structure CdS/EDA (protonated) hybrid nanowires with rich surface sulfur (S) vacancies via a facile solvothermal method for efficient CO_2 photoreduction. The advantages of this CdS/EDA (protonated) nanowires with rich S vacancies are threefold. First, the unique 3D structure of hybrid nanowires is highly favorable for the photocatalytic reaction because of the strengthened visible light capture capability, high specific surface area and accessible porosities. Second, protonated EDA molecules in the hybrid nanowires act as electron donors can well restrain charge recombination by capturing photogenerated holes, and the amino groups in EDA can immensely promote the CO_2 capture. Lastly and most importantly, the S vacancies can further promote the separation of surface photogenerated carriers, specifically promote the hydrogen adsorption as well as accelerate CO_2 adsorption and activation over the surface of CdS/EDA nanowires. As a result, under visible light irradiation, the CO and H_2 formation rates of 3D CdS/EDA nanowires with rich S vacancies are 115.6 and 959.4 μmol g^{-1} h^{-1} (CO: H_2 = 1: 8.3), much higher than that of bulk CdS, CdS/EDA and 3D CdS/EDA nanowires with poor sulfur vacancies, respectively. Based on characterization analyses and theoretical calculations, the possible mechanism of CO_2 photoreduction to syngas for this system is further revealed.

2. Experiments

2.1. Catalysts synthesis

2.1.1. Synthesis of bulk CdS and CdS/EDA

The bulk CdS was prepared via a solvothermal process. Typically, cadmium acetate dihydrate (1 mmol) and thiourea (1 mmol) were first dissolved in deionized water (30 mL) with continuous stirring for 20 min. Then, The obtained solution was poured into a 50 mL Teflon-lined autoclave and maintained at 150 °C for 10 h. The obtained precipitates were washed several times by deionized water and ethanol after the autoclave cooled to room temperature. Finally, the products were dried in an oven at 60 ℃ for 24 h to obtain bulk CdS. The preparation procedure of CdS/EDA was similar to that of the bulk CdS, with exception of the starting materials that were dissolved in the misted solution of deionized water (22 mL) and ethylenediamine (8 mL).

2.1.2. Synthesis of V_S-P-CdS/EDA NW and V_S-R-CdS/EDA NW

In a typical procedure, cadmium acetate dihydrate (1 mmol), thiourea (2 mmol) and polyvinylpyrrolidone (0.03 g) were mixed in deionized water (5 mL) and ethylenediamine (25 mL) solution under stirring for 20 min. Then, the obtained solution was poured into a 50 mL Teflon-lined autoclave and maintained at 100 ℃ for 20 h. The obtained precipitates were washed several times by deionized water and ethanol after the autoclave cooled to room temperature. Finally, the products were dried by vacuum freeze drying and designated as V_S-R-CdS/EDA NW. And the procedure of the 3D CdS/EDA nanowires with poor S vacancies was similar to that of the V_S-R-CdS/EDA NW except that thiourea was added in solution at 1 mmol, and then the obtained product was named V_S-P-CdS/EDA NW.

2.2. Characterizations

The morphologies of samples were investigated by scanning electron microscopy (SEM, Sigma 500) and transmission electron microscopy (TEM, JEM 200CX), EDS mapping was attached to the SEM. The BET surface area of samples were investigated by N_2 adsorption using a Quadrasorb 2MP surface area analyzer. The crystallographic structures of samples were examined on a Bruker D8 powder X-ray diffractometer. The Fourier transform infrared (FT-IR) spectra were obtained through Nicolet IN10 spectrometer. The surface electronic states and valence band (VB) of catalysts were carried out by X-ray photoelectron spectroscopy (XPS). The electron paramagnetic resonance (EPR) spectra were acquired by a Germany Bruke A300 spectrometer. Raman measurements were performed on a Horiba IHR550 spectrometer at 532 nm excitation wavelength. The UV–Vis diffuse reflection spectra (DRS) were tested at a PerkinElmer 750 s spectrophotometer. The photoluminescence (PL) spectra (excited under 400 nm) and time-resolved photoluminescence spectroscopy (TRPL) were performed by a FLS1000 fluorescence spectrophotometer. The CO_2 adsorption isotherms were measured on a TriStar II 3020 apparatus at 298 K. Temperature-programmed desorption (TPD) measurements of CO_2 and CO were carried out on a AutoChem II 2920 chemisorption analyser. The in-situ Fourier transfer infrared spectra (FT-IR) were carried out on a Nicolet IS50 spectrometer. The electrochemical measurements were performed on a CHI660E electrochemistry workstation. The working electrode was prepared through the coating of photocatalysts on a FTO glass with the effective area of 1 cm^2. Pt wires was used as the counter electrode, and saturated Ag/AgCl as the reference electrode. The measurements were carried out in the Na_2SO_4 solution (0.5 M, pH = 6.8) at room temperature.

2.3. Photocatalytic activity evaluation

The reactions of CO_2 photoreduction were carried out on a Labsolar-6A closed gas system (Perfectlight, China). Typically, the prepared photocatalysts (15 mg), acetonitrile (20 mL), triethanolamine (4 mL) and H_2O (5 mL) were equably dispersed on the bottom of reactor with the volume of 240 mL. After vacuum treatment of the reaction system for several times, the high purity CO_2 (99.999%) was filled into the reaction system to reach an ambient pressure. After storing in the darkness for 3.0 h to reach the adsorption-desorption equilibrium of CO_2 on the mixture surface, the reactor was then irradiated by a 300 W Xe lamp ($\lambda > 420$ nm). During the photocatalytic reaction, the mixture in the reactor was continuously stirred by a magnetic stirrer. Within a given time interval (1 h), 1 mL gas was extracted from the reactor for products analysis by a gas chromatograph (Shimadzu, GC-2014). The isotope experiments were measured on the gas chromatography-mass spectrometry (GC-MS, GC-7900, MS5977A).

2.4. DFT calculations

The density functional theory (DFT) calculations were carried out by using Vienna Ab initio Simulation Package (VASP) [25]. The electron-ion interactions were treated by projector augmented wave (PAW), and the Perdew-Burke-Ernzerhof (PBE) pseudopotential within the generalized gradient approximation (GGA) was used to treat exchange-correlation function [26,27]. K-sampling used the Monkhorst-Pack mesh of 5 × 5 × 1 (9 ×9 ×1 was used in the calculation of density of state (DOS)). Meanwhile, the cutoff energy, maximum force and energy convergence tolerance on each atom were set to be 500 eV, 0.05 eV $Å^{-1}$ and 10^{-5} eV, respectively. All periodic slabs have a vacuum layer of at least 15 Å to construct a slab model of CdS layers (002 surface). An ethylenediamine molecule was loaded on the surface CdS to model the CdS/EDA hybrid materials. The adsorption energy and free energy changes of reaction intermediates could be calculated by the following Eqs. (1) and (2):

$$\Delta E = E_{ads} - E_{*} \quad (1)$$

$$\Delta G = \Delta E + \Delta E_{ZPE} - T\Delta S \quad (2)$$

where ΔE_{ZPE} is the zero-point energy change, ΔS is the entropy change and T is the temperature (T = 298.15 K). And the values of ΔE_{ZPE} and ΔS were computed by vibration frequency.

3. Results and discussion

3.1. CdS/EDA nanowires 3D network structure with S vacancies

The V_S-R-CdS/EDA NW was synthesized by a facile solvothermal approach as schematically described in Fig. 1a. Firstly, EDA molecules are protonated by reacting with water at 100 °C to form positively charged ammonium ions, and followed the protonated EDA molecules are combined into adjoining CdS layers through coordination with S

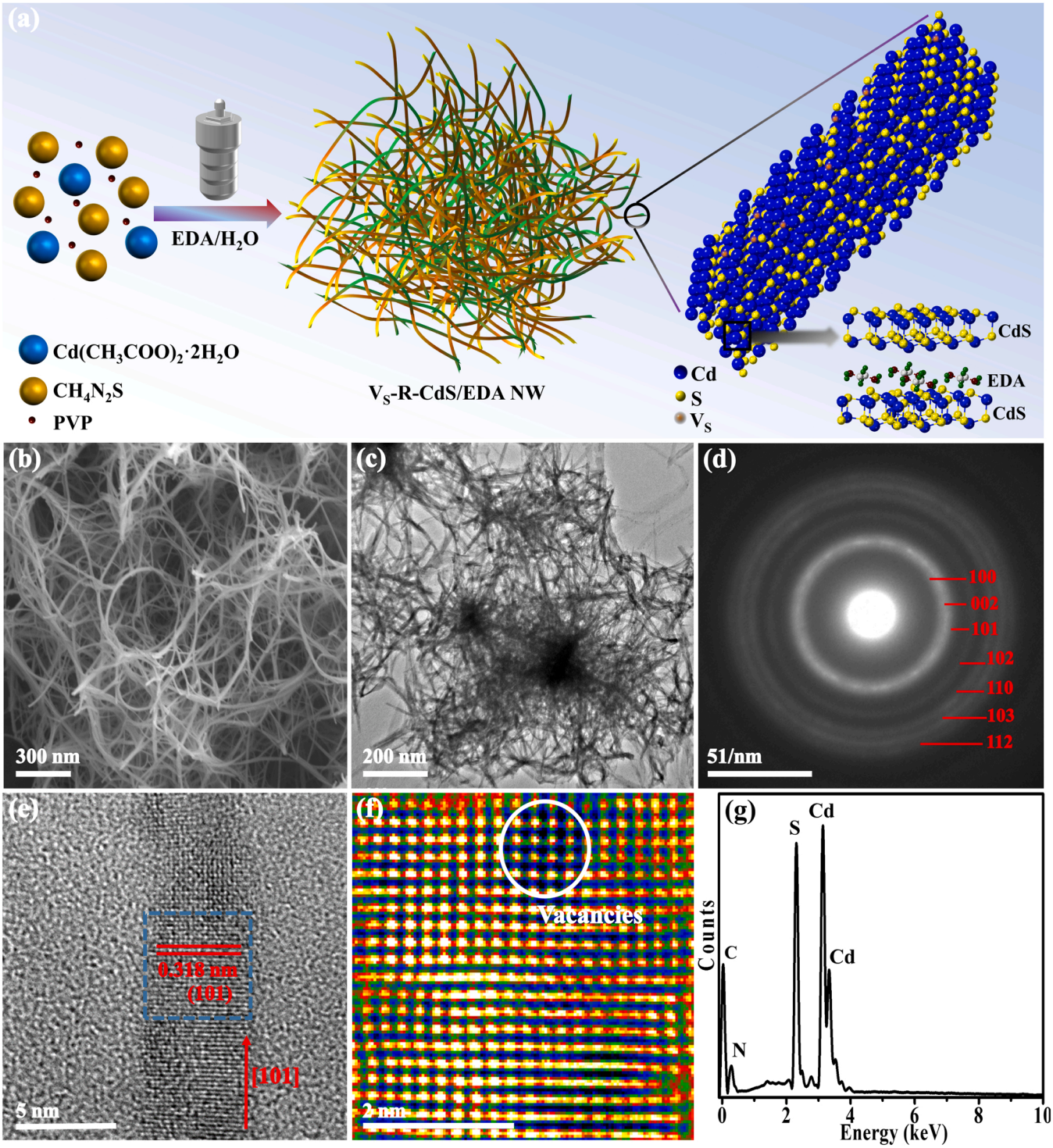

Fig. 1. (a) Schematic diagram for the synthesis of V_S-R-CdS/EDA NW. (b) SEM image, (c) TEM image, (d) Electron diffraction patterns and (e) HRTEM image of V_S-R-CdS/EDA NW. (f) False-color image of the HRTEM image of the region outlined in (e) for V_S-R-CdS/EDA NW. (g) EDS pattern of V_S-R-CdS/EDA NW.

atoms [14,28]. Meanwhile, excess thiourea can be adsorbed on the surface of primary nanocrystals, partially blocking the directional growth of crystals and the low synthesis temperature, resulting in the formation of rich vacancies structure [29,30]. Finally, 3D network structure CdS/EDA (protonated) hybrid nanowires with rich S vacancies are constructed by modification of EDA molecules. And the prepared all samples are shown in Fig. S1. Benefiting from the unique 3D network structure assembled by nanowires, V_S-P-CdS/EDA NW and V_S-R-CdS/EDA NW not only exhibit obvious pore structure, but also have large specific surface area (Fig. S2). As shown in Table S1, V_S-R-CdS/EDA NW has the largest specific surface area of 112.1 $m^2 g^{-1}$, which is 57.7, 7.2 and 1.1 times higher than that of bulk CdS (1.94 $m^2 g^{-1}$), CdS/EDA (15.49 $m^2 g^{-1}$) and V_S-P-CdS/EDA NW (95.37 $m^2 g^{-1}$), respectively. It demonstrates that the 3D network structure can endow V_S-R-CdS/EDA NW with more active sites and stronger solar light capture ability.

The crystallographic structures of bulk CdS, CdS/EDA, V_S-P-CdS/EDA NW and V_S-R-CdS/EDA NW were examined by the X-ray diffraction (XRD) analysis as shown in Fig. S3. The XRD diffraction peaks of all samples at $2\theta = 24.9°$, 26.6°, 28.2°, 43.7°, 47.8° and 51.9° are indexed to (100), (002), (101), (110), (103) and (112) planes of hexagonal CdS (JCPDS No. 41-1049) [31], respectively. And there are no apparent impurities in the all samples. It is obvious that the intensity of the diffraction peaks of bulk CdS, CdS/EDA, V_S-P-CdS/EDA NW and V_S-R-CdS/EDA NW gradually weakened, which mainly attributed to the smaller crystalline grain size [32]. The molecular structure of V_S-R-CdS/EDA NW was further analyzed by Fourier transform infrared (FTIR) spectra (Fig. S4). As for bulk CdS, the peaks at 1070 and 1380 cm^{-1} are attributed to the Cd—S bond [33], the peaks at 1640 and 3430 cm^{-1} originate from the surface-adsorbed water molecules of catalysts [33]. Meanwhile, the characteristic peaks of CdS are also observed in the V_S-R-CdS/EDA NW. Additionally, the peaks at 1033, 1330 and 1492 cm^{-1} for V_S-R-CdS/EDA NW are assigned to -NH_2, -NH and -CH_2 [34,35], respectively. It's worth noting that V_S-R-CdS/EDA NW has a sharper peak at 3440 cm^{-1} compared to bulk CdS, which may be related to the N-H stretching vibration due to the presence of EDA molecules [35].

The morphologies and microstructures of all samples were observed by SEM and TEM measurements (Figs. 1b–g and S5). As illustrated in Fig. S5a–d, bulk CdS presents irregular blocks with a large size of several micrometers and CdS/EDA is irregular particles with a smaller size of dozens to several hundred nanometers. V_S-R-CdS/EDA NW and V_S-P-CdS/EDA NW show 3D network nanowires structure with diameters of around 25 nm and 40 nm, respectively (Figs. 1b, c and S5e, f). Meanwhile, the corresponding SAED pattern (Fig. 1d) confirms that the polycrystalline structure of V_S-R-CdS/EDA NW. And the HRTEM image (Fig. 1e) reveals that V_S-R-CdS/EDA NW has the ordered lattice fringes with the interplanar spacing of 0.318 nm, corresponding to the (101) crystal plane of hexagonal CdS [36], which implying that the nanowires grow along the [101] direction. In addition, from the false-color image of the HRTEM image in Fig. 1f, it can be observed that evident atomic absence in the white region suggests that the existence of numerous vacancies in the V_S-R-CdS/EDA NW. Moreover, the EDS image (Fig. 1g) verifies that V_S-R-CdS/EDA NW is composed of S, Cd, C and N elements.

The presence of S vacancies in V_S-P-CdS/EDA NW and V_S-R-CdS/EDA NW was identified using the XPS spectra (Fig. 2a, b). In the bulk CdS and CdS/EDA samples, the S 2p XPS spectrum can be deconvoluted into two peaks at 161.1 and 162.3 eV, which are ascribed to S^{2-} [37].

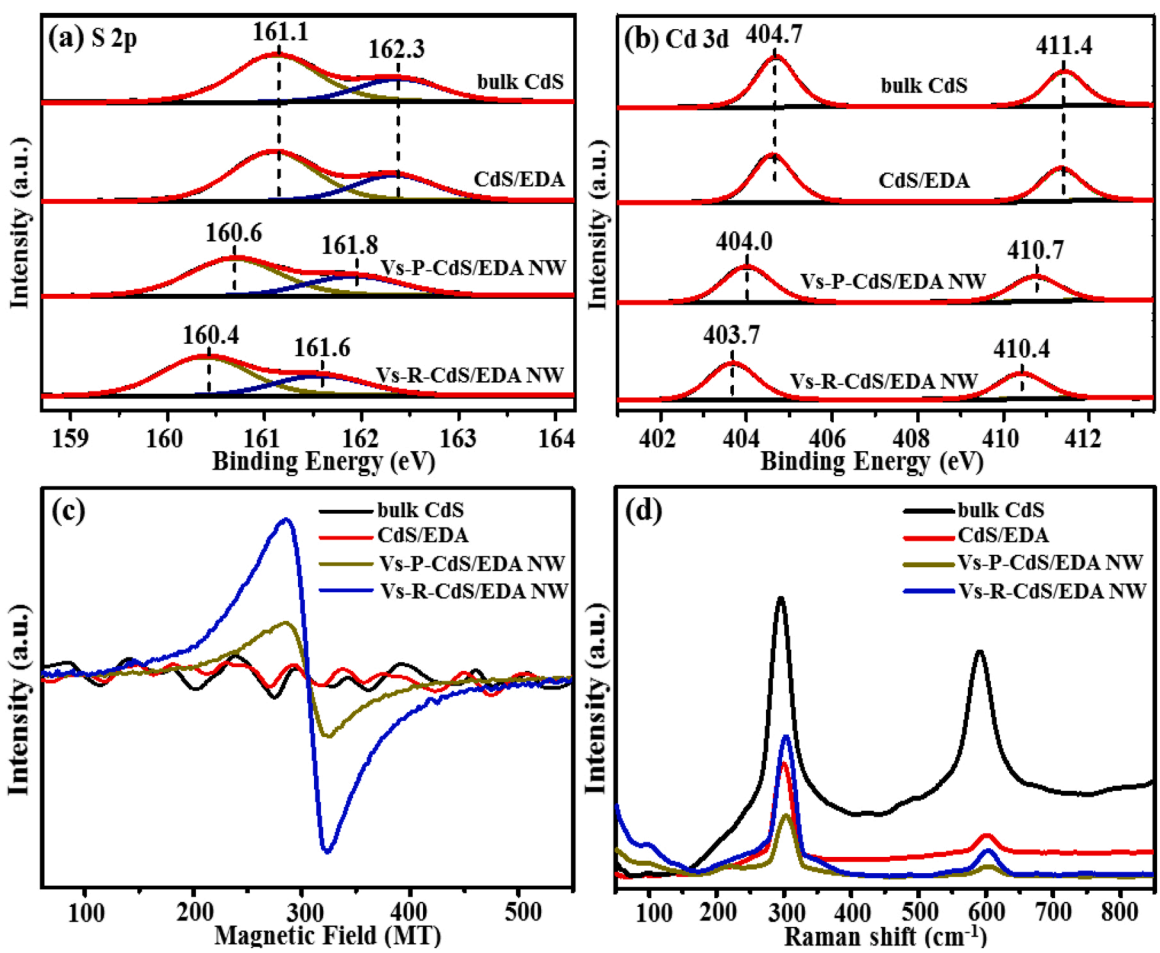

Fig. 2. (a) S 2p XPS spectra, (b) Cd 3d XPS spectra, (c) EPR spectra and (d) Raman spectra of bulk CdS, CdS/EDA, V_S-P-CdS/EDA NW and V_S-R-CdS/EDA NW.

Compared with bulk CdS and CdS/EDA, the S 2p peaks binding energy of V_S-P-CdS/EDA NW (160.6 eV, 161.8 eV) and V_S-R-CdS/EDA NW (160.4 eV, 161.6 eV) become lower gradually, indicating that there are S vacancies in the samples and the higher concentration of S vacancies in V_S-R-CdS/EDA NW due to lower coordination S [37,38]. The Cd 3d XPS spectrum of bulk CdS and CdS/EDA samples can be deconvoluted into two peaks at 404.7 and 411.4 eV, which belong to Cd $3d_{5/2}$ and Cd $3d_{3/2}$ [39]. However, the Cd 3d peaks of V_S-P-CdS/EDA NW (404.0 ev, 410.7 eV) and V_S-R-CdS/EDA NW (403.7 ev, 410.4 eV) shift to lower binding energy regions, which can be attributed to the increase of electron cloud density of Cd^{2+} in the S vacancies region [37]. Furthermore, the room-temperature electron paramagnetic resonance (EPR) spectra has been carried out to further confirm the existence of S vacancies in the samples. As shown in Fig. 2c, it's obvious that there is no EPR signal in bulk CdS and CdS/EDA, and V_S-R-CdS/EDA NW displays the higher EPR intensity (g = 2.001) than that of V_S-P-CdS/EDA NW, indicating the higher concentration of unpaired electrons in V_S-R-CdS/EDA NW with abundant S vacancies [38,40]. Fig. 2d displays the Raman spectra of the all samples at the excitation wavelength of 532 nm. The peaks at about 300 and 600 cm^{-1} are attributed to the first-order (1LO) and second-order (2LO) modes of CdS, respectively [7]. Compared with bulk CdS, the intensity ratio of 2LO to 1LO (I_{2LO}/I_{1LO}) for the other samples decreased significantly due to the reduction of samples size (Table S2) [41]. In addition, the Raman intensity of V_S-R-CdS/EDA NW is slightly higher than that of CdS/EDA and V_S-P-CdS/EDA NW, which is likely due to the presence of rich S vacancies [42].

3.2. Optimized energy band structure and faster charge carriers separation over 3D CdS/EDA nanowires with S vacancies

The UV–vis diffuse reflectance spectra of all photocatalysts are shown in Fig. 3a. The light absorption threshold of bulk CdS is 582 nm, its optical bandgap can be calculated to be 2.13 eV (Fig. 3b) [36]. The light absorption edges of CdS/EDA, V_S-P-CdS/EDA NW and V_S-R-CdS/EDA NW show significantly blue shift in comparison with bulk CdS, which may be caused by the different atomic configurations on each surface and special inorganic-organic hybrid structures [14,43], and the corresponding bandgaps are 2.18, 2.37 and 2.35 eV (Fig. 3b), respectively. Fig. 3c reveals the valance band (VB) potentials of bulk CdS, CdS/EDA, V_S-P-CdS/EDA NW and V_S-R-CdS/EDA NW are 1.53, 1.38, 1.13 and 1.08 eV vs NHE, respectively. On the basis of formula $E_{CB} = E_{VB} - E_g$ [33], the conduction band (CB) potentials are calculated to be −0.60, −0.80, −1.24 and −1.27 eV for bulk CdS, CdS/EDA, V_S-P-CdS/EDA NW and V_S-R-CdS/EDA NW, respectively. In addition, the flatband potential (V_{fb}) of samples were estimated by the Mott–-Schottky curves as shown in Fig. S6. The positive tangent slopes of the straight lines reveal that all the samples are n-type semiconductors [44], and the V_{fb} potentials of bulk CdS, CdS/EDA, V_S-P-CdS/EDA NW and V_S-R-CdS/EDA NW are determined to be −0.58, −0.88, −1.02 and −0.92 V (vs Ag/AgCl), respectively. Although the V_{fb} potentials of samples are different from that the CB values, it also shows that the

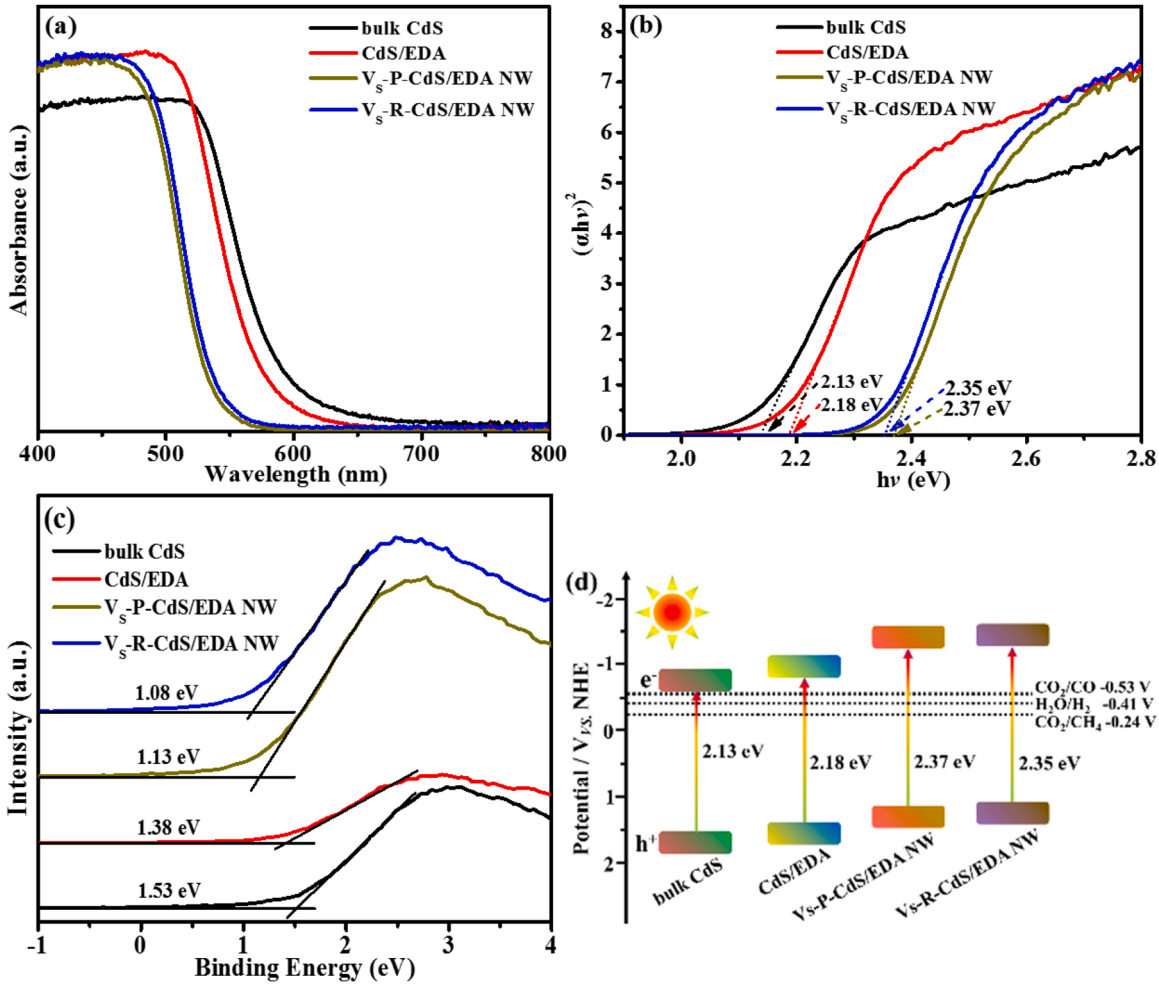

Fig. 3. (a) UV–vis DRS, (b) $(\alpha h\nu)^2$ versus ($h\nu$) plots, (c) valence band XPS and (d) band gap structures vs NHE of bulk CdS, CdS/EDA, V_S-P-CdS/EDA NW and V_S-R-CdS/EDA NW.

synergistic effect of 3D structure, EDA molecules and S vacancies in the CdS leads to a similar negative shift at the V_{fb} potentials of catalysts. Thermodynamically, the more negative the conduction band value of a semiconductor is, the stronger its reduction ability is [45]. Although bulk CdS has a wider absorption range of visible light, its CB value is too positive. And EDA molecules can elevate the CB edge of CdS, thus improving its reduction driving force. Notably, CdS/EDA nanowires with S vacancies have a more negative CB potential, this also shows V_S-R-CdS/EDA NW has a very good potential for CO_2 photoreduction (Fig. 3d).

To further explore the effect of introducing S vacancies into 3D CdS/EDA nanowires on the electronic structure of the catalysts, the theoretical models of CdS, CdS/EDA and CdS/EDA with S vacancies were established, and their density of states were conducted by the DFT calculations (Fig. 4). It can be observed that the both VB and CB of CdS, CdS/EDA and V_S-CdS/EDA are mainly contributed by the S orbital and Cd orbital. However, the CB of CdS/EDA and V_S-CdS/EDA is also made up of a little N orbital. In addition, compared to CdS, the density of states of CdS/EDA and V_S-CdS/EDA increased gradually, thus adding more charge carriers [46]. Moreover, the existence of S vacancies results in the emergence of new defect levels (the shaded blue part in Fig. 4e), indicating that the higher carrier concentration and easier electron transition, which effectively improve the conductivity and charge separation efficiency of V_S-R-CdS/EDA NW [22]. And the green part of density of states in Fig. 4e indicates that the introduction of S vacancies significantly enhances the electron density states near the CB edge, which is beneficial to the reduction reaction.

The separation efficiency of photogenerated carriers is an essential factor to affect the activity of photocatalysts, so we investigated the charge recombination behavior of all photocatalysts. The PL emission spectra of all samples were collected with the excitation wavelength of 400 nm (Fig. 5a). The emission peak of bulk CdS and CdS/EDA samples

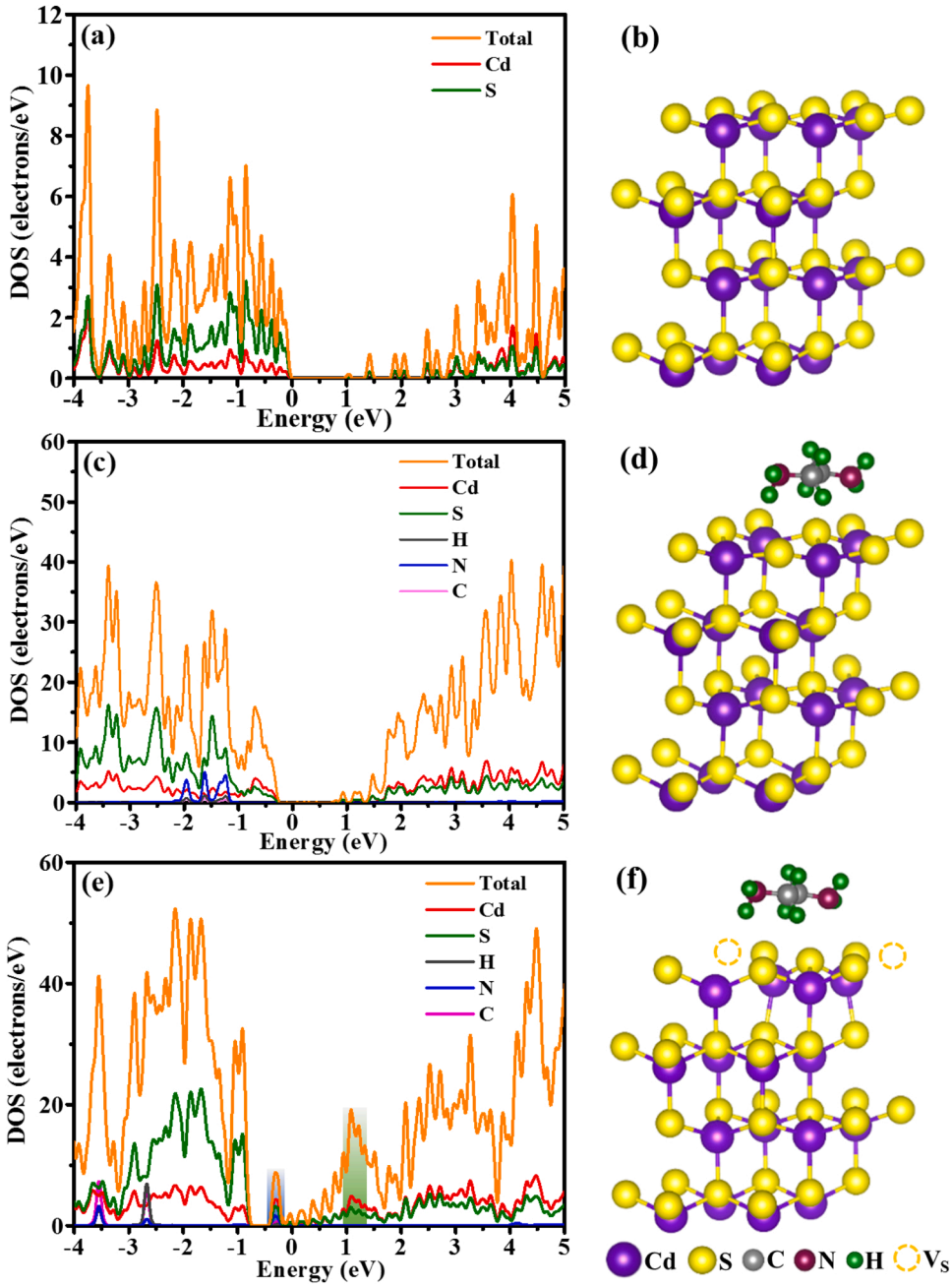

Fig. 4. The geometric structures of (b) CdS, (d) CdS/EDA and (f) V_S-CdS/EDA. The density of states of (a) bulk CdS, (c) CdS/EDA and (e) V_S-CdS/EDA.

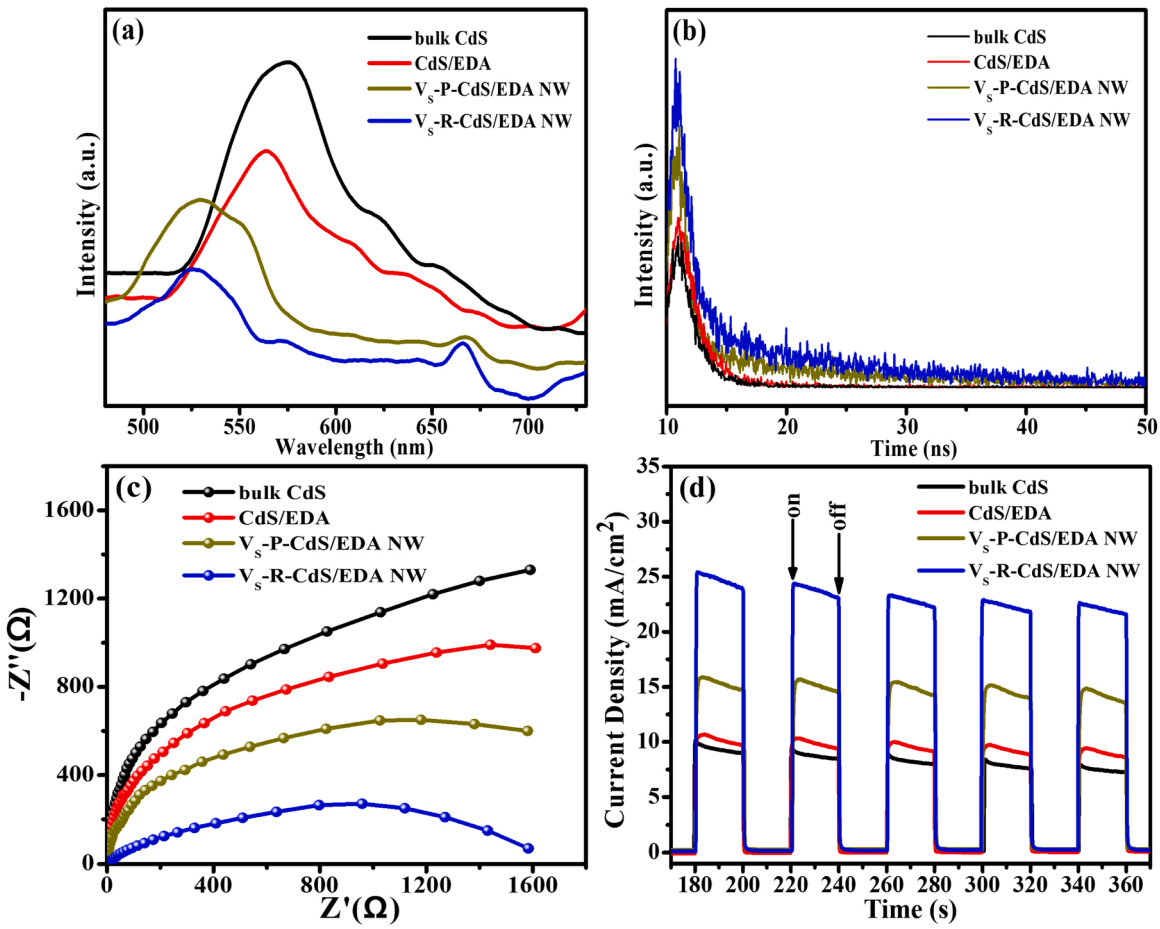

Fig. 5. (a) Steady-state PL emission spectra, (b) time-resolved transient PL decay spectra, (c) EIS spectra and (d) transient photocurrent response of bulk CdS, CdS/EDA, V_S-P-CdS/EDA NW and V_S-R-CdS/EDA NW.

at ~570 nm is assigned to the band to band transition in CdS [44], while V_S-P-CdS/EDA NW and V_S-R-CdS/EDA NW exhibit an obvious blue-shift to ~525 nm and consistent with the UV analysis result. And the PL emission peak in V_S-R-CdS/EDA is almost quenched as expressed by the greatly reduced peak intensity compared to that of bulk CdS, CdS/EDA and V_S-P-CdS/EDA, which indicates its effectively suppressed electron-hole pair recombination rate. In addition, the weak emission peak at 665 nm of V_S-P-CdS/EDA NW and V_S-R-CdS/EDA NW can be arised from the surface S vacancies of the CdS [47]. As shown in Fig. 5b and Table 1, the average fluorescent lifetime (τ) of samples can be calculated through the follow formula [46]: $\tau = A_1\tau_1^2 + A_2\tau_2^2/(A_1\tau_1 + A_2\tau_2)$, where τ_1, τ_2 are the fluorescent lifetime and A_1, A_2 stand for amplitudes. The average fluorescent lifetime of V_S-R-CdS/EDA NW ($\tau = 4.05$ ns) is longer than that of bulk CdS ($\tau = 1.53$ ns), CdS/EDA ($\tau = 2.07$ ns) and V_S-P-CdS/EDA NW ($\tau = 3.03$ ns). The longer lifetime of V_S-R-CdS/EDA NW is likely ascribed to the role of EDA molecules in providing electron donors can consume the photogenerated holes to reduce the charge recombination, and 3D network nanowire structure enables the photogenerated carriers to migrate rapidly from the inside to the surface [14,24]. In addition, the surface S vacancies can trap photogenerated electrons and further enhance the charge separation, resulting in the lifetime of carriers is prolonged [46].

Table 1
The TRPL decay data of bulk CdS, CdS/EDA, V_S-P-CdS/EDA NW and V_S-R-CdS/EDA NW.

Samples	τ_1 (ns)	A_1 (%)	τ_2 (ns)	A_2 (%)	τ (ns)
bulk Cds	0.38	75.4	2.16	24.6	1.53
Cds/EDA	0.45	73.4	2.79	26.8	2.07
Vs-P-Cds/EDA NW	0.59	68.7	3.86	31.3	3.03
Vs-R-Cds/EDA NW	0.72	64.1	4.92	35.9	4.05

Furthermore, the charge transport property of photocatalysts was evaluated by electrochemical impedance spectroscopy (EIS) (Fig. 5c). The diameter of the semicircular Nyquist curve in the order of bulk CdS > CdS/EDA > V_S-P-CdS/EDA NW > V_S-R-CdS/EDA NW, implying much smaller charge transfer resistance and the faster interfacial charge transfer process in V_S-R-CdS/EDA NW. Moreover, the V_S-R-CdS/EDA NW exhibits the highest transient photocurrent density (Fig. 5d), which is 2.2, 2.1, and 1.10 times higher than that of bulk CdS, CdS/EDA and V_S-P-CdS/EDA NW, respectively, it reveals the most fastest interfacial charge separation and migration efficiency of V_S-R-CdS/EDA NW photocatalyst, which can be attributed to surface amino modification, 3D network nanowires structure and abundant S vacancies in the V_S-R-CdS/EDA NW. This also means the possibility of higher photocatalytic activity for V_S-R-CdS/EDA NW.

3.3. Enhanced photocatalytic activity for syngas production and photocatalytic mechanism over 3D CdS/EDA nanowires with S vacancies

The photocatalytic CO_2 reduction experiments for syngas production were performed under visible light irradiation. The main gas phase products are CO, H_2 and trace CH_4 (Fig. 6a–c). As shown in Fig. 6d, V_S-R-CdS/EDA NW shows excellent CO formation rate of 115.6 μmol g^{-1} h^{-1}, which is 39.8, 12.7 and 1.94 fold higher than that of bulk CdS (2.9 μmol g^{-1} h^{-1}), CdS/EDA (9.1 μmol g^{-1} h^{-1}) and V_S-P-CdS/EDA NW (59.3 μmol g^{-1} h^{-1}), respectively. Meanwhile, V_S-R-CdS/EDA NW also shows excellent H_2 generation rate of 959.4 μmol g^{-1} h^{-1}, which is

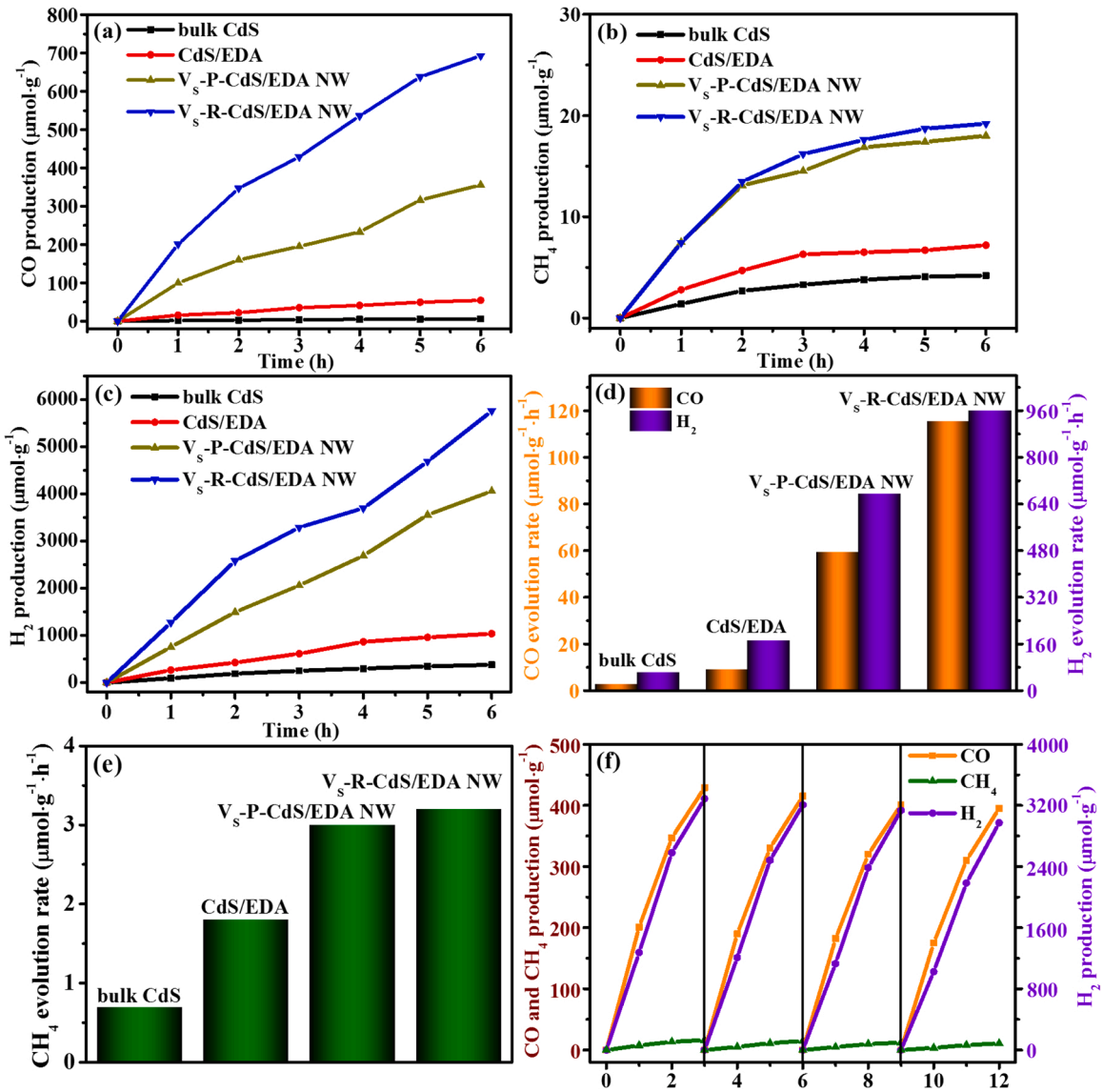

Fig. 6. Photocatalytic (a) CO, (b) CH_4 and (c) H_2 evolution of bulk CdS, CdS/EDA, V_S-P-CdS/EDA NW and V_S-R-CdS/EDA NW. Average gas production rates of (d) CO, H_2 and (e) CH_4 for bulk CdS, CdS/EDA, V_S-P-CdS/EDA NW and V_S-R-CdS/EDA NW. (f) Recycling experiments of V_S-R-CdS/EDA NW during every 3 h of reaction time.

superior to the H_2 generation rates of bulk CdS (62.9 μmol g^{-1} h^{-1}), CdS/EDA (173.9 μmol g^{-1} h^{-1}) and V_S-P-CdS/EDA NW (676.3 μmol$g^{-1}h^{-1}$). Importantly, the total production of syngas after 6 h reaction is up to 6449 μmol for V_S-R-CdS/EDA NW, and V_S-R-CdS/EDA NW also exhibits a higher CO/H_2 ratio of 1: 8.3 (Table S3), which is beneficial to the subsequent thermochemical conversions including methanation and Fischer-Tropsch process [4]. Also, photoreduction CO_2 performance of V_S-R-CdS/EDA NW is compared with that of other reported CdS-based photocatalysts (Table S4). In addition, the yields of CO and H_2 for V_S-R-CdS/EDA NW remains almost unchanged after four cycles of reaction in the whole 12 h (Fig. 6f). The color change of V_S-R-CdS/EDA NW before and after the photocatalytic reaction is shown in Fig. S7. And the crystal structure of V_S-R-CdS/EDA NW after photocatalytic reaction shows no significant difference from that of the primeval sample (Fig. S8), which further indicates that V_S-R-CdS/EDA NW has excellent durability for CO_2 photoreduction to produce CO and H_2. What's more, H_2 was detected and ^{13}C-isotope labeled CO_2 experiment over V_S-R-CdS/EDA NW was carried out to determine the origin of carbon element of reaction products (Fig. S9). The strong peaks at $m/z = 17$ and $m/z = 29$ can be ascribed to $^{13}CH_4$ and ^{13}CO in the mass spectra [48], respectively, confirming that the generated products are completely derived from CO_2 feedstock.

The adsorption capacity of photocatalyst for CO_2 is the vital factor affecting its CO_2 reduction efficiency, so the CO_2 adsorption isotherms of as-prepared samples were investigated at 297 K under 1 atm (Fig. 7a). V_S-R-CdS/EDA NW exhibits the maximum CO_2 uptake of 5.18 cm^3 g^{-1}, higher than that of bulk CdS (0.67 cm^3 g^{-1}), CdS/EDA (1.8 cm^3 g^{-1}) and V_S-P-CdS/EDA NW (4.01 cm^3 g^{-1}), indicating that the synergistic effect of amino modification, 3D network structure and S vacancies in V_S-R-CdS/EDA NW effectively promotes the adsorption of CO_2. Meanwhile, the CO_2 temperature-programmed desorption (TPD) analysis depicts that V_S-R-CdS/EDA NW demonstrates a strong CO_2 activation ability with a stronger peak at the range of 200–450 °C (Fig. 7b), which is much higher than that of bulk CdS (250–320 °C), CdS/EDA (250–350 °C) and V_S-P-CdS/EDA NW (250–400 °C), indicating that the 3D structure, EDA molecules and S vacancies can be favorable for CO_2 adsorption on V_S-R-CdS/EDA NW. In addition, in order to deeply investigate the reaction process of CO_2 photoreduction, the in-situ FT-IR spectra of CO_2 photoreduction over V_S-R-CdS/EDA NW sample were carried out under Xe lamp irradiation as displayed in Fig. 7c. Several broad absorption peaks

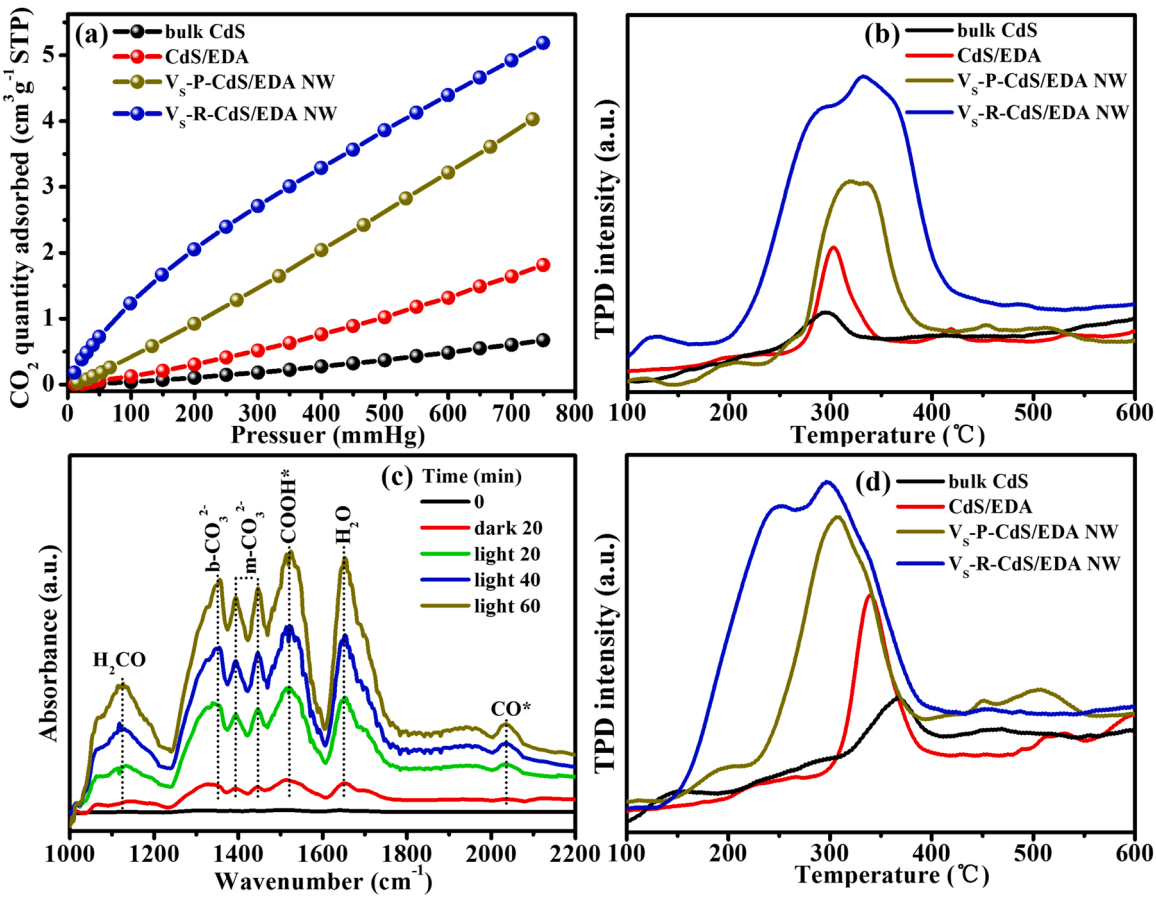

Fig. 7. (a) CO_2 adsorption isotherms and (b) CO_2-TPD of bulk CdS, CdS/EDA, VS-P-CdS/EDA NW and VS-R-CdS/EDA NW (c) In-situ FT-IR spectra for CO_2 photoreduction on VS-R-CdS/EDA NW (d) CO-TPD of bulk CdS, CdS/EDA, VS-P-CdS/EDA NW and VS-R-CdS/EDA NW.

at 1115, 1353, 1393, 1446 and 1650 cm^{-1} are assigned to H_2CO, b-CO_3^{2-}, m-CO_3^{2-}, m-$CO_3^{2-}$and H_2O [49–52], respectively. Additionally, it is worth noting that the absorption peak at 1524 cm^{-1} is indicative of COOH* species, which are the critical intermediate during the conversion of CO_2 to CO [53]. Specifically, it can be observed that the CO* peak at 2015 cm^{-1}, which belongs to the dissociative absorption of CO_2 [50]. The intensities of these peaks are progressively increased with extended light irradiation time, signifying the continuous conversion of CO_2 into CO over V_S-R-CdS/EDA NW. What's more, the stronger and lower temperature CO desorption peak of V_S-R-CdS/EDA NW also indicates that the CO* species are easier to desorb from its surface (Fig. 7d), further confirms the improved CO_2 photoreduction activity of V_S-R-CdS/EDA NW.

In addition, in order to explore the structure-property relationship for introduction of S vacancies in the 3D CdS/EDA nanowires on improving its performance of CO_2 photoreduction at the surface molecular level, the DFT calculations further reveal the detailed process of CO_2-to-CO conversion over V_S-CdS/EDA via *CO_2 → *COOH → *CO → CO (Fig. 8a). As expected, the advantage of EDA-decoration is conductive to CO_2 adsorption as illustrated by the reduced absorption energy of CO_2 on CdS/EDA (−0.20 eV) compared to CdS (−0.06 eV). This absorption energy can be further decreased to −0.26 eV on S vacancy engineered CdS/EDA, suggesting that S vacancies can greatly improve the CO_2 adsorption on the surface of CdS/EDA as well. Notably, it can also be seen from the difference charge density that the introduction of S vacancies on the surface of CdS can improve the binding strength with CO_2 and promote the charge transfer between CO_2 and V_S-CdS/EDA. What's more, the C—O bond of the adsorbed CO_2 on V_S-CdS/EDA is more easily activated with a bond length of 1.212 Å, markedly longer than the value of CO_2 on CdS (1.177 Å) and CdS/EDA (1.180 Å) [53,54]. The free energy diagram of CO_2 reduction to CO is shown in Fig. 8b. In the reaction process, the generation of *CO is the rate-determining step of the photoreaction, which has the highest energy barrier. The energy barrier for *CO formation on V_S-CdS/EDA is 0.46 eV, much lower than that on CdS (1.16 eV) and CdS/EDA (0.74 eV), beneficial to the further protonation of *COOH to produce CO. Meanwhile, the desorption of *CO is an exothermic process on all catalysts. Therefore, V_S-R-CdS/EDA NW shows a high activity of photoreduction of CO_2 to CO.

Considering that H_2 is the main component of syngas mixtures, we also calculated the free energy of hydrogen adsorption for CdS, CdS/EDA and V_S-CdS/EDA (Fig. 8c). And it seems that *H is adsorbed on the surface of CdS, not on the EDA molecule, and *H prefers to interact with S vacancies (Fig. S10). The closer the free energy of hydrogen adsorption for the catalyst is to zero, the higher its HER activity is [55]. It is found that the free energy of hydrogen adsorption for V_S-CdS/EDA is 0.19 eV, which shows much more favorable H_2 evolution activity than that of CdS (−1.07 eV) and CdS/EDA (−0.85 eV), suggesting that the synergistic effect of organic amine modification and S vacancies can effectively adjust the electronic structure of CdS and boost the interaction between CdS surface and H_2O (or H_3O^+) [56], thus achieving the splendid photocatalytic H_2 evolution activity. Therefore, the theoretical calculation results show that V_S-R-CdS/EDA NW can effectively promote hydrogen adsorption and activate CO_2 activation to achieve high-efficiency syngas production.

Based on the experimental and theoretical calculation results, the possible CO_2 photoreduction mechanism of V_S-R-CdS/EDA NW is proposed in Fig. 9. The excited electronic in the VB of V_S-R-CdS/EDA is transited to its CB under the visible light irradiation, resulting in the formation of holes in the VB, thus generating photogenerated electron-hole pairs [18,57]. Then the surface S vacancies of V_S-R-CdS/EDA NW

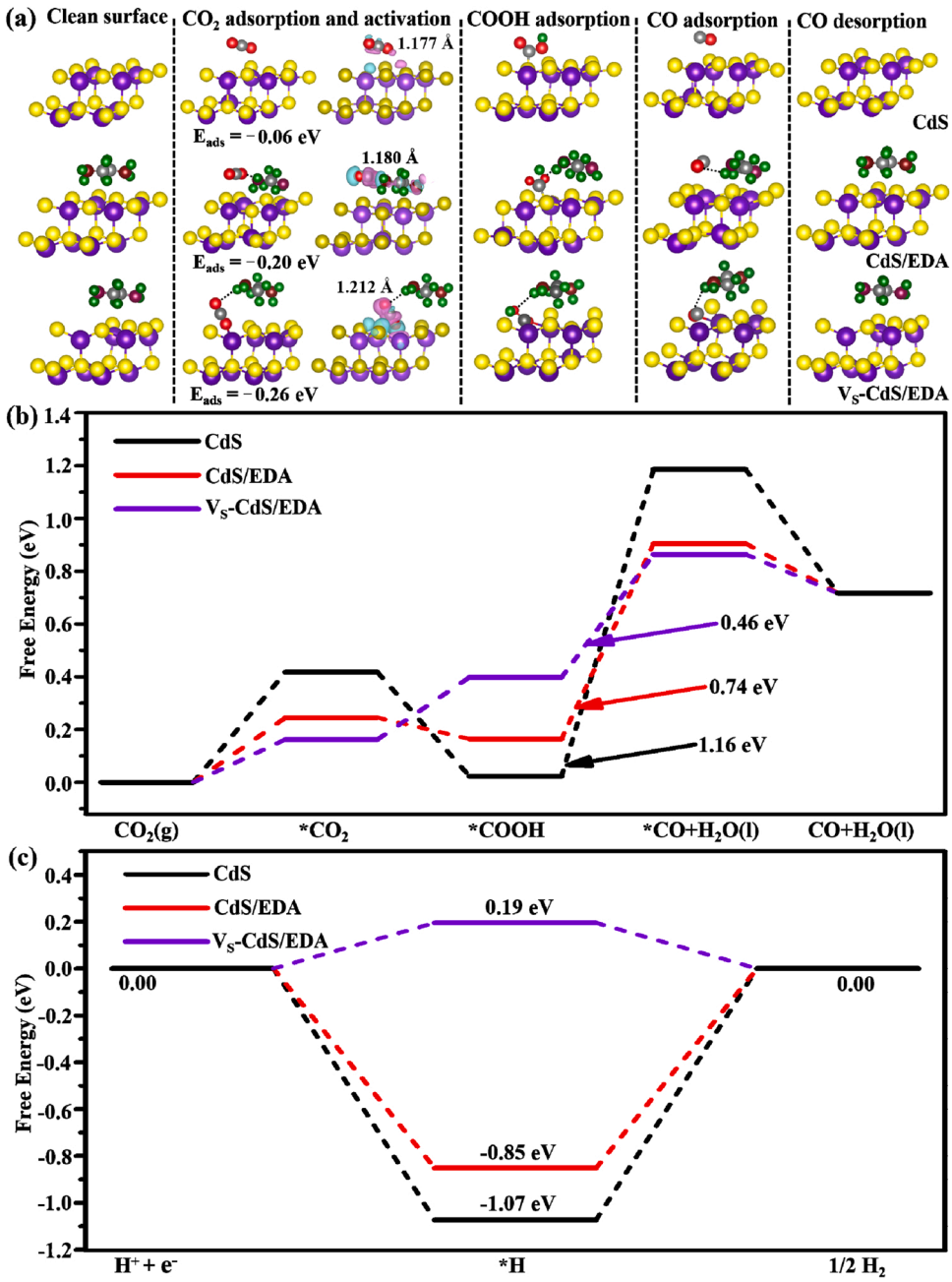

Fig. 8. (a) Schematic illustration for CO_2 reduction to CO pathway over CdS, CdS/EDA and V_S-CdS/EDA. The free energy diagram of (b) CO_2-to-CO and (c) HER over the surface of CdS, CdS/EDA and V_S-CdS/EDA.

can capture the photoinduced electrons, leading to an efficient separation of photogenerated carriers [46]. And the rich surface S vacancies of 3D hybrid nanowires offer abundant coordinatively unsaturated sites cooperate with EDA molecules to effectively adsorb CO_2 [23,35]. Meanwhile, the photogenerated electrons on the S vacancies are transferred to the adsorbed $*CO_2$. In addition, H_2O is dissociated into H^+ and OH^- on the surface. Subsequently, the photogenerated electrons react with H^+ to produce H_2, and the adsorbed $*CO_2$ reacts with photogenerated electrons and H^+ to generate *COOH intermediate [23]. Finally, *COOH intermediate generates CO and CH_4 through further protonation, and the holes on the VB are consumed by TEOA.

4. Conclusion

In summary, 3D network structure CdS/EDA nanowires with rich S vacancies were prepared via a low temperature solvothermal route. With reinforced visible light captation, shorter carriers migration distance to the surface of the photocatalyst and accelerated carriers separation and transport, as well as amino modification and plentiful coordinatively unsaturated active sites for efficient hydrogen adsorption and CO_2 adsorption and activation, and thus V_S-R-CdS/EDA NW is found to be a highly efficient photocatalyst for a high ratio of CO/H_2 syngas production under the exposure to visible light. This work presents the advantages of synergetic effect of 3D structure, molecular decoration and vacancy engineering on enhancing the efficiency of CO_2 photoreduction to produce syngas.

CRediT authorship contribution statement

Tong Tian: Conceptualization, Data curation, Investigation,

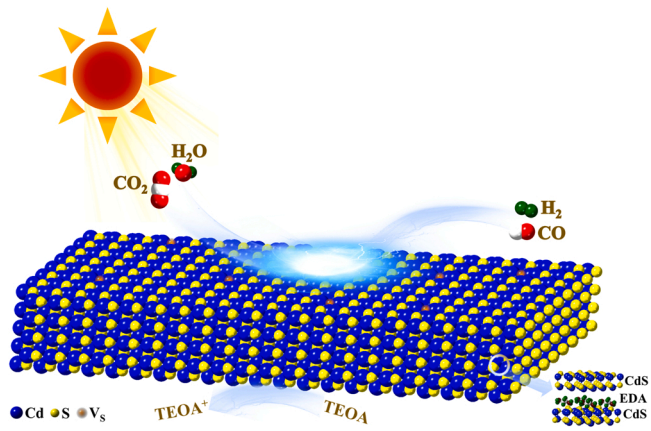

Fig. 9. Schematic representation of CO_2 photoreduction over V_S-CdS/EDA NW.

Methodology, Software, Writing – original draft, Writing – review & editing. **Xiaoyan Jin:** Investigation, Resources, Supervision. **Neng Guo:** Investigation, Resources. **Huiquan Li:** Funding acquisition, Project administration, Resources, Supervision, Validation, Writing – review & editing. **Yan Han:** Investigation, Funding acquisition, Resources. **Yupeng Yuan:** Resources, Supervision, Validation, Writing – review & editing.

Declaration of Competing Interest

The authors declare that they have no known competing financial interests or personal relationships that could have appeared to influence the work reported in this paper.

Acknowledgments

This work is financially supported by National Natural Science Foundation of China (51872003), Natural Science Foundation of Anhui Province in China (gxgwfx2018059, KJ2020ZD47), Key Research and Development Programs of Anhui Province (202104i07020011), Horizontal Cooperation Project of Fuyang Municipal Government – Fuyang Normal University (SXHZ202003, SXHZ202102) and School Level Key Project of Fuyang Normal University (2020FSKJ03ZD).

Appendix A. Supplementary material

Supplementary data associated with this article can be found in the online version at doi:10.1016/j.apcatb.2022.121227.

References

[1] S. Gao, Y. Lin, X.C. Jiao, Y.F. Sun, Q.Q. Luo, W.H. Zhang, D.Q. Li, J.L. Yang, Y. Xie, Partially oxidized atomic cobalt layers for carbon dioxide electroreduction to liquid fuel, Nature 529 (2016) 68–71.
[2] S.F. Ji, Y. Qu, T. Wang, Y.J. Chen, G.F. Wang, X. Li, J.C. Dong, Q.Y. Chen, W. Y. Zhang, Z.D. Zhang, S.Y. Liang, R. Yu, Y. Wang, D.S. Wang, Y.D. Li, Rare-earth single erbium atoms for enhanced photocatalytic CO_2 reduction, Angew. Chem. Int. Ed. 59 (2020) 10651–10657.
[3] X.M. Cheng, X.Y. Dao, S.Q. Wang, J. Zhao, W.Y. Sun, Enhanced photocatalytic CO_2 reduction activity over NH_2-MIL-125(Ti) by facet regulation, ACS Catal. 11 (2021) 650–658.
[4] H.Z. Yang, D.R. Yang, X. Wang, POM-incorporated CoO nanowires for enhanced photocatalytic syngas production from CO_2, Angew. Chem. Int. Ed. 59 (2020) 15527–15531.
[5] C. Han, Y.H. Li, J.Y. Li, M.Y. Qi, Z.R. Tang, Y.J. Xu, Cooperative syngas production and C−N bond formation in one photoredox cycle, Angew. Chem. Int. Ed. 60 (2021) 7962–7970.
[6] P. Zhang, S.B. Wang, B.Y. Guan, X.W. Lou, Fabrication of CdS hierarchical multi-cavity hollow particles for efficient visible light CO_2 reduction, Energy Environ. Sci. 12 (2019) 164–168.
[7] C.B. Bie, B.C. Zhu, F.Y. Xu, L.Y. Zhang, J.G. Yu, In situ grown monolayer N-doped graphene on CdS hollow spheres with seamless contact for photocatalytic CO_2 reduction, Adv. Mater. 31 (2019), 1902868.
[8] Z.L. Wang, Y.F. Chen, L.Y. Zhang, B. Cheng, J.G. Yu, J.J. Fan, Step-scheme CdS/TiO_2 nanocomposite hollow microsphere with enhanced photocatalytic CO_2 reduction activity, J. Mater. Sci. Technol. 56 (2020) 143–150.
[9] J.R. Ran, M. Jaroniec, S.Z. Qiao, Cocatalysts in semiconductor-based photocatalytic CO_2 reduction: achievements, challenges, and opportunities, Adv. Mater. 30 (2018), 1704649.
[10] T.T. Kong, Y.W. Jiang, Y.J. Xiong, Photocatalytic CO_2 conversion: what can we learn from conventional CO_x hydrogenation, Chem. Soc. Rev. 49 (2020) 6579–6591.
[11] S. Chandrasekaran, L. Yao, L.B. Deng, C. Bowen, Y. Zhang, S.M. Chen, Z.Q. Lin, F. Peng, P.X. Zhang, Recent advances in metal sulfides: from controlled fabrication to electrocatalytic, photocatalytic and photoelectrochemical water splitting and beyond, Chem. Soc. Rev. 48 (2019) 4178–4280.
[12] Y. Qi, Y. Zhao, Y.Y. Gao, D. Li, Z. Li, F.X. Zhang, C. Li, Redox-based visible-light-driven Z-scheme overall water splitting with apparent quantum efficiency exceeding 10%, Joule 2 (2018) 2393–2402.
[13] W. Zhang, X.Y. Pan, P.Q. Long, X.T. Liu, X. Long, Y. Yu, Z.G. Yi, Platinum nanoparticles supported on defective tungsten bronze-type $KSr_2Nb_5O_{15}$ as a novel photocatalyst for efficient ethylene oxidation, J. Mater. Chem. A 5 (2017) 18998–19006.
[14] J.L. Lv, J. Liu, J.F. Zhang, K. Dai, C.H. Liang, Z.L. Wang, G.P. Zhu, Construction of organic-inorganic cadmium sulfide/diethylenetriamine hybrids for efficient photocatalytic hydrogen production, J. Colloid Interface Sci. 512 (2018) 77–85.
[15] J.B. Jakobsen, M.H. Ronne, K. Daasbjerg, T. Skrydstrup, Are amines the holy grail for facilitating CO_2 reduction, Angew. Chem. Int. Ed. 60 (2021) 9174–9179.
[16] M.J. Lashaki, S. Khiavi, A. Sayari, Stability of amine-functionalized CO_2 adsorbents: a multifaceted puzzle, Chem. Soc. Rev. 48 (2019) 3320–3405.
[17] F. Chen, Z.Y. Ma, L.Q. Ye, T.Y. Ma, T.R. Zhang, Y.H. Zhang, H.W. Huang, Macroscopic spontaneous polarization and surface oxygen vacancies collaboratively boosting CO_2 photoreduction on $BiOIO_3$ single crystals, Adv. Mater. 32 (2020), 1908350.
[18] Y.Q. He, H. Rao, K.P. Song, J.X. Li, Y. Yu, Y. Lou, C.G. Li, Y. Han, Z. Shi, S.H. Feng, 3D hierarchical $ZnIn_2S_4$ nanosheets with rich Zn vacancies boosting photocatalytic CO_2 reduction, Adv. Funct. Mater. 29 (2019), 1905153.
[19] B.B. Dong, J.Y. Cui, Y. Qi, F.X. Zhang, Nanostructure engineering and modulation of (oxy)nitrides for application in visible-light-driven water splitting, Adv. Mater. 33 (2021), 2004697.
[20] M. Xiao, L. Zhang, B. Luo, M.Q. Lyu, Z.L. Wang, H.M. Huang, S.C. Wang, A.J. Du, L. Z. Wang, Molten-salt-mediated synthesis of an atomic nickel Co-catalyst on TiO_2 for improved photocatalytic H_2 evolution, Angew. Chem. Int. Ed. 59 (2020) 7230–7234.
[21] J. Li, X.Y. Wu, W.F. Pan, G.K. Zhang, H. Chen, Vacancy-rich monolayer BiO_{2-x} as a highly efficient UV, visible, and near-infrared responsive photocatalyst, Angew. Chem. Int. Ed. 57 (2018) 491–495.
[22] J. Di, X.X. Zhao, C. Lian, M.X. Ji, J.X. Xia, J. Xiong, W. Zhou, X.Z. Cao, Y.B. She, H. L. Liu, K.P. Loh, S.J. Pennycook, H.M. Li, Z. Liu, Atomically-thin Bi_2MoO_6 nanosheets with vacancy pairs for improved photocatalytic CO_2 reduction, Nano Energy 61 (2019) 54–59.
[23] Y.X. Li, M.M. Wen, Y. Wang, G. Tian, C.Y. Wang, J.C. Zhao, Plasmonic hot electrons from oxygen vacancies for infrared light-driven catalytic CO_2 reduction on Bi_2O_{3-x}, Angew. Chem. Int. Ed. 60 (2021) 910–916.
[24] W.J. Luo, X.J. Chen, Z. Wei, D. Liu, W.Q. Yao, Y.F. Zhu, Three-dimensional network structure assembled by g-C_3N_4 nanorods for improving visible-light photocatalytic performance, Appl. Catal. B Environ. 255 (2019), 117761.
[25] G. Kresse, J. Furthmuller, Efficient iterative schemes for ab initio total-energy calculations using a plane-wave basis set, Phys. Rev. B 54 (1996) 11169–11186.
[26] P.E. Blochl, Projector augmented-wave method, Phys. Rev. B 50 (1994) 17953–17979.
[27] J.P. Perdew, K. Burke, M. Ernzerhof, Generalized gradient approximation made simple, Phys. Rev. Lett. 77 (1996) 3865–3868.
[28] M.R. Gao, W.T. Yao, H.B. Yao, S.H. Yu, Synthesis of unique ultrathin lamellar mesostructured $CoSe_2$−amine (protonated) nanobelts in a binary solution, J. Am. Chem. Soc. 131 (2009) 7486–7487.
[29] J.F. Xie, H. Zhang, S. Li, R.X. Wang, X. Sun, M. Zhou, J.F. Zhou, X.W. Lou, Y. Xie, Defect-rich MoS_2 ultrathin nanosheets with additional active edge sites for enhanced electrocatalytic hydrogen evolution, Adv. Mater. 25 (2013) 5807–5813.
[30] J.F. Xie, J.J. Zhang, S. Li, F. Grote, X.D. Zhang, H. Zhang, R.X. Wang, Y. Lei, B. C. Pan, Y. Xie, Controllable disorder engineering in oxygen-incorporated MoS_2 ultrathin nanosheets for efficient hydrogen evolution, J. Am. Chem. Soc. 135 (2013) 17881–17888.
[31] G.Q. Han, Y.H. Jin, R.A. Burgess, N.E. Dickenson, X.M. Cao, Y.J. Sun, Visible-light-driven valorization of biomass intermediates integrated with H_2 production catalyzed by ultrathin Ni/CdS nanosheets, J. Am. Chem. Soc. 139 (2017) 15584–15587.
[32] Y.Y. Xie, X.T. Shang, D. Liu, H.B. Zhao, Y.Y. Gu, Z.Z. Zhang, X.X. Wang, Non-noble metal thickness-tunable Bi_2MoO_6 nanosheets for highly efficient visible-light-driven nitrobenzene reduction into aniline, Appl. Catal. B Environ. 259 (2019), 118087.
[33] X.Q. Wu, J. Zhao, L.P. Wang, M.M. Han, M.L. Zhang, H.B. Wang, H. Huang, Y. Liu, Z.H. Kang, Carbon dots as solid-state electron mediator for $BiVO_4$/CDs/CdS Z-scheme photocatalyst working under visible light, Appl. Catal. B Environ. 206 (2017) 501–509.
[34] J.D. Hu, J. Xie, W. Jia, S. Zhang, S.Q. Wang, K. Wang, Y.L. Cao, Interesting molecule adsorption strategy induced energy band tuning: boosts 43 times photocatalytic Water splitting ability for commercial TiO_2, Appl. Catal. B Environ. 268 (2020), 118753.

[35] N.N. Meng, C.B. Liu, Y. Liu, Y.F. Yu, B. Zhang, Efficient electrosynthesis of syngas with tunable CO/H_2 ratios over $Zn_xCd_{1-x}S$-amine inorganic-organic hybrids, Angew. Chem. Int. Ed. 58 (2019) 18908–18912.
[36] S. Song, J.F. Qu, P.J. Han, M.J. Hulsey, G.P. Zhang, Y.Z. Wang, S. Wang, D.Y. Chen, J.M. Lu, N. Yan, Visible-light-driven amino acids production from biomass-based feedstocks over ultrathin CdS nanosheets, Nat. Commun. 11 (2020) 4899.
[37] L. Cheng, Y.H. Li, A.P. Chen, Y.H. Zhu, C.Z. Li, Impacts on carbon dioxide electroreduction of cadmium sulfides via continuous surface sulfur vacancy engineering, Chem. Commun. 56 (2020) 563–566.
[38] C.Y. Jiang, X.X. Xu, M.L. Mei, F.N. Shi, Coordination polymer derived sulfur vacancies rich CdS composite photocatalyst with nitrogen doped carbon as matrix for H_2 production, ACS Sustain. Chem. Eng. 6 (2018) 854–861.
[39] P. Zhou, Q.H. Zhang, Z.K. Xu, Q.Y. Shang, L. Wang, Y.G. Chao, Y.J. Li, H. Chen, F. Lv, Q. Zhang, L. Gu, S.J. Guo, Atomically dispersed Co-P3 on CdS nanorods with electron-rich feature boosts photocatalysis, Adv. Mater. 32 (2020), 1904249.
[40] Y. Yin, J.C. Han, Y.M. Zhang, X.H. Zhang, P. Xu, Q. Yuan, L. Samad, X.J. Wang, Y. Wang, Z.H. Zhang, P. Zhang, X.Z. Cao, B. Song, S. Jin, Contributions of phase, sulfur vacancies, and edges to the hydrogen evolution reaction catalytic activity of porous molybdenum disulfide nanosheets, J. Am. Chem. Soc. 138 (2016) 7965–7972.
[41] V. Singh, P.K. Sharma, P. Chauhan, Surfactant mediated phase transformation of CdS nanoparticles, Mater. Chem. Phys. 121 (2010) 202–207.
[42] L.Z. Lju, X.L. Wu, F. Gao, J.C. Shen, T.H. Li, P.K. Chu, Determination of surface oxygen vacancy position in SnO_2 nanocrystals by Raman spectroscopy, Solid State Commun. 151 (2011) 811–814.
[43] J.G. Yu, Y.F. Yu, P. Zhou, W. Xiao, B. Cheng, Morphology-dependent photocatalytic H_2-production activity of CdS, Appl. Catal. B Environ. 156–157 (2014) 184–191.
[44] R. Shi, H.F. Ye, F. Liang, Z. Wang, K. Li, Y.X. Weng, Z.S. Lin, W.F. Fu, C.M. Che, Y. Chen, Interstitial P-doped CdS with long-lived photogenerated electrons for photocatalytic water splitting without sacrificial agents, Adv. Mater. 30 (2018), 1705941.
[45] X. Li, J.G. Yu, M. Jaroniec, X.B. Chen, Cocatalysts for selective photoreduction of CO_2 into solar fuels, Chem. Rev. 119 (2019) 3962–4179.
[46] C. Du, Q. Zhang, Z.Y. Lin, B. Yan, C.X. Xia, G.W. Yang, Half-unit-cell $ZnIn_2S_4$ monolayer with sulfur vacancies for photocatalytic hydrogen evolution, Appl. Catal. B Environ. 248 (2019) 193–201.
[47] Z.M. Liu, G.L. Liu, X.L. Hong, Influence of surface defects and palladium deposition on the activity of CdS nanocrystals for photocatalytic hydrogen production, Acta Phys. Chim. Sin. 35 (2019) 215–222.
[48] F.Y. Xu, K. Meng, B.C. Zhu, H.B. Liu, J.S. Xu, J.G. Yu, Graphdiyne: a new photocatalytic CO_2 reduction cocatalyst, Adv. Funct. Mater. 29 (2019), 1904256.
[49] Y. Li, B.H. Li, D.N. Zhang, L. Cheng, Q.J. Xiang, Crystalline carbon nitride supported copper single atoms for photocatalytic CO_2 reduction with nearly 100% CO selectivity, ACS Nano 14 (2020) 10552–10561.
[50] Y.P. Liu, D.Y. Shen, Q. Zhang, Y. Lin, F. Peng, Enhanced photocatalytic CO_2 reduction in H_2O vapor by atomically thin Bi_2WO_6 nanosheets with hydrophobic and nonpolar surface, Appl. Catal. B Environ. 283 (2021), 119630.
[51] L.J. Liu, Y.Q. Jiang, H.L. Zhao, J.T. Chen, J.L. Cheng, K.S. Yang, Y. Li, Engineering coexposed {001} and {101} facets in oxygen-deficient TiO_2 nanocrystals for enhanced CO_2 photoreduction under visible light, ACS Catal. 6 (2016) 1097–1108.
[52] X.Y. Xiong, C.L. Mao, Z.J. Yang, Q.H. Zhang, G.I.N. Waterhouse, L. Gu, T.R. Zhang, Photocatalytic CO_2 reduction to CO over Ni single atoms supported on defect-rich Zirconia, Adv. Energy Mater. 10 (2020), 2002928.
[53] X.L. Jin, C.D. Lv, X. Zhou, L.Q. Ye, H.Q. Xie, Y. Liu, H. Su, B. Zhang, G. Chen, Oxygen vacancy engineering of $Bi_{24}O_{31}Cl_{10}$ for boosted photocatalytic CO_2 conversion, ChemSusChem 12 (2019) 2740–2747.
[54] Y.B. Shi, G.M. Zhan, H. Li, X.B. Wang, X.F. Liu, L.J. Shi, K. Wei, C.C. Ling, Z.L. Li, H. Wang, C.L. Mao, X. Liu, L.Z. Zhang, Simultaneous manipulation of bulk excitons and surface defects for ultrastable and highly selective CO_2 photoreduction, Adv. Mater. 33 (2021), 2100143.
[55] W.H. Feng, J. Yuan, L.L. Zhang, W.T. Hu, Z.H. Wu, X.L. Wang, X.Y. Huang, P. Liu, S.Y. Zhang, Atomically thin ZnS nanosheets: facile synthesis and superior piezocatalytic H_2 production from pure H_2O, Appl. Catal. B Environ. 277 (2020), 119250.
[56] Z. Luo, R. Miao, T.D. Huan, I.M. Mosa, A.S. Poyraz, W. Zhong, J.E. Cloud, D.A. Kriz, S. Thanneeru, J.K. He, Y.S. Zhang, R. Ramprasad, S.L. Suib, Mesoporous MoO_{3-x} material as an efficient electrocatalyst for hydrogen evolution reactions, Adv. Energy Mater. 6 (2016), 1600528.
[57] Y. Jiang, H.Y. Ning, C.G. Tian, B.J. Jiang, Q. Li, H.J. Yan, X.L. Zhang, J.Q. Wang, L. Q. Jing, H.G. Fu, Single-crystal TiO_2 nanorods assembly for efficient and stable cocatalyst-free photocatalytic hydrogen evolution, Appl. Catal. B Environ. 229 (2018) 1–7.